RSC Advances

PAPER

View Article Online
View Journal | View Issue

Cite this: *RSC Adv.*, 2019, **9**, 17246

Facile fabrication of a novel $BiPO_4$ phase junction with enhanced photocatalytic performance towards aniline blue degradation†

Ahmed B. Azzam,[a] S. M. El-Sheikh,[*b] R. A. Geioushy,[b] Bahaa Ahmed Salah,[a] Farida M. El-Dars[a] and Ahmed S. Helal[c]

Received 26th March 2019
Accepted 16th May 2019

DOI: 10.1039/c9ra02315a

rsc.li/rsc-advances

A novel $BiPO_4$ photocatalyst has been fabricated *via* a facile precipitation route using dimethyl sulfoxide (DMSO) as a solvent. The physical and chemical properties of the $BiPO_4$ photocatalyst material were analyzed using XRD, Rietveld refinements XRD, FE-SEM, TEM, HR-TEM, EDS, XPS, FT-IR, Raman spectra, UV-Vis (DRS), and PL. The results confirm that hexagonal phase $BiPO_4$ (HBIP) nanorods were successfully synthesized. FE-SEM images reveal that the addition of surfactant "CTAB" during preparation can control the surface morphology of $BiPO_4$. The Rietveld refinement technique revealed the formation of a monazite monoclinic (nMBIP) and monoclinic (mMBIP) phase junction resulting from the calcination of HBIP at 500 °C. The photocatalytic behavior of the as-synthesized hexagonal and monoclinic $BiPO_4$ nanostructures towards aniline blue (AB) degradation under UV light was systematically investigated. Among all catalysts, the phase junction (nMBIP–mMBIP) structure demonstrated the highest photocatalytic activity. The degradation rate of AB over the (nMBIP–mMBIP) phase junction structure was 3.4 times higher than that by HBIP. These results suggested that the surface-phase junction provides a synergistic effect for the electron–hole transfer process.

1. Introduction

Nowadays, photocatalysts are widely used for solving environmental and energy issues.[1–4] Semiconductors such as g-C_3N_4,[5,6] CdS,[7] Ag_3VO_4,[8] ZnO,[9] and TiO_2 (ref. 10–12) have been employed in dealing with the emergence of environmental pollution issues. Among the above-mentioned photocatalysts, bismuth-based photocatalysts have attracted considerable attention for environmental and energy related applications.[13] $BiPO_4$ has a wide band gap (3.5–4.6 eV), while incorporation with nonmetal oxy-acid displayed an efficient photocatalytic dye degradation compared to TiO_2 (P25).[14] The limited absorption of $BiPO_4$ is one of the major drawbacks for widespread applications.[15] Developing an efficient and stable $BiPO_4$ photocatalyst continues to be a challenging endeavor. This can take place *via* hetero-junctions with other semiconductors,[16,17] and doping with nonmetals.[18] Recently, semiconductor photocatalysts with phase junctions have played a dominant role in photocatalytic degradation.[19] $BiPO_4$ exists in three crystal structures; hexagonal (HBIP), monazite monoclinic (nMBIP), and monoclinic (mMBIP).[20] In all crystal structures of $BiPO_4$, bismuth is bonded with eight near neighbor oxygen atoms, while phosphorus is associated with four oxygen atoms.[21] Furthermore, hexagonal $BiPO_4$ (HBIP) has been transformed into (nMBIP–mMBIP) phases under calcination at different temperatures.[22] It is reported that nMBIP–mMBIP phase junction structure provide an enhancement in the photocatalytic activity.[15,23] Herein, $BiPO_4$ with different morphologies was synthesized by facile precipitation method followed by calcination of HBIP at different temperatures to form a (nMBIP–mMBIP) phase junction structure. To the best of our knowledge, separation of the two monoclinic phases has been investigated by Rietveld refinements. In addition, the photocatalytic behavior under UV light was assessed by aniline blue (AB) degradation for the first time. Meanwhile, the photocatalytic mechanism is discussed.

[a]*Chemistry Department, Faculty of Science, Helwan University, Helwan, Egypt*

[b]*Nanomaterials and Nanotechnology Department, Advanced Materials Division, Central Metallurgical R & D Institute (CMRDI), P. O. Box 87, Helwan, 11421 Cairo, Egypt. E-mail: selsheikh2001@gmail.com; saidelsheikh@cmrdi.sci.eg; Tel: +20 1022316076*

[c]*Department of Nuclear Science and Engineering, Massachusetts Institute of Technology, 77 Massachusetts Avenue, Cambridge, MA 02139, USA*

† Electronic supplementary information (ESI) available. See DOI: 10.1039/c9ra02315a

2. Experimental

2.1 Materials

Bismuth nitrate pentahydrate [$Bi(NO_3)_3 \cdot 5H_2O$, 99.99%], diammonium hydrogen phosphate [$(NH_4)_2HPO_4$ > 99.0%], dimethylsulfoxide (DMSO > 99.9%) and cetyltrimethylammonium bromide (CTAB, 98%) were delivered from Sigma-Aldrich.

2.2 Synthesis of $BiPO_4$ nanostructures

A simple precipitation route is developed to prepare $BiPO_4$ photocatalyst. Briefly, 1.94 g of bismuth nitrate and 0.5 g cetyltrimethylammonium bromide (CTAB) were dissolved in 40 ml dimethylsulfoxide (DMSO), and stirred for 30 min to obtain a clear solution. A 0.524 g $(NH_4)_2HPO_4$ was dissolved in 40 ml double distilled water, and added slowly to the above mixture under vigorous stirring for 1 h. After that, centrifuged to collect white precipitate of $BiPO_4$ (HBIP), washed with ethanol and water. Dried in oven at 90 °C for 6 h. Calcination of $BiPO_4$ (HBIP) sample was investigated at different temperatures in the range from 400 to 600 °C, under constant heating rate (2 °C min^{-1} for 2 h). Also, $BiPO_4$ photocatalyst was synthesized without CTAB.

2.3 Characterization

X-ray diffraction data (XRD) were acquired on Bruker, Axs D8, using Cu-Kα radiation, $\lambda = 1.5406$ Å, with 2θ ranging from 15° to 55° and scan rate of 2° min^{-1}, Germany. Rietveld refinements XRD were carried out on Panalytical X-Pert pro diffractometer (XRPD) with a Cu target, and a conventional 1.8 kW sealed X-ray tube source. Quanta FEG-250 SEM with 20 kV accelerated voltage and transmission electron microscopy (TEM, JEOLJEM-1230, Japan) are used as a diagnostic tool for morphology study. For mapping EDS, an energy dispersive X-ray spectroscopy were analyzed by JEOL 2010 TEM. The specific surface area of the as-synthesized photocatalysts, after degassing at 170 °C for 3 h, were determined by N_2 adsorption–desorption based Brunauer–Emmett–Teller (BET) and Barret–Joyner–Halenda (BJH) curves using (Quantachrome NOVA instrument, USA). The elemental composition and the oxidation state were characterized by XPS and recorded on PHI Versa probe II, using monochromatic Al Kα (15.0 kV with kinetic energy of 1486.6 eV). Raman scattering spectra measurements were collected with using Bruker, senterra dispersive micro-Raman at 532 nm Nd:YAG laser source, Germany. The vibration spectrum of $BiPO_4$ samples were performed by Fourier Infrared absorption spectrometer FT-IR using PerkinElmer Spectrum (200–4000 cm^{-1}). UV-Vis Spectrophotometer, Jasco-V-570 was used to collect the absorption spectra of $BiPO_4$ samples. The photoluminescence (PL) spectrum was analyzed using RF-5310 PC spectrofluorophotometer, Shimadzu.

2.4 Photocatalytic performance test

The photocatalytic activity of the hexagonal and monoclinic $BiPO_4$ photocatalysts was evaluated by aniline blue degradation under UV irradiation. In details, 0.05 g $BiPO_4$ photocatalyst was suspended in 100 ml of (AB) dye (20 ppm), and stirred vigorously in darkness for 30 min. The photodegradation process was performed using UV lamp (20 W–254 nm) at room temperature. After each 20 min, approximately 3 ml liquid sample was withdrawn, and centrifuged for 10 min at 4000 rpm. The AB concentration was measured spectrophotometry at 606 nm. The calculated degradation (%) was carried out using the following formula:

$$\text{Degradation } (\%) = [C_0 - C_t]/C_0 \times 100\%$$

where C_0 and C_t refer to the initial dye concentration after dark experiment and concentration at time (t) min, respectively.

3. Results and discussions

3.1 Characterization of $BiPO_4$

The crystal and phase compositions of the as-prepared $BiPO_4$ photocatalysts were analyzed by XRD technique as presented in Fig. 1a. Evidently, $BiPO_4$ photocatalysts prepared in DMSO or DMSO/CTAB have the same diffraction peaks at 2-theta angles 20.1°, 25.5°, 29.5°, 31.3°, 37.8°, 41.9°, 47.3° and 48.7° which correspond to the crystal orientations of (101), (110), (200), (102), (112), (211), (301) and (212) planes of $BiPO_4$, respectively. These results agreed with JCPDS card no. 15-0766.[4] Obviously, there is no significant difference in the $BiPO_4$ samples prepared with and without CTAB. Further, the diffraction patterns were ascribed to the $BiPO_4$ hexagonal phase (HBIP, space group: $P3_121$), and no impurity peaks were detected, indicates the crystallinity nature. The as-prepared hexagonal $BiPO_4$ sample prepared in DMSO/CTAB was calcined at different temperatures

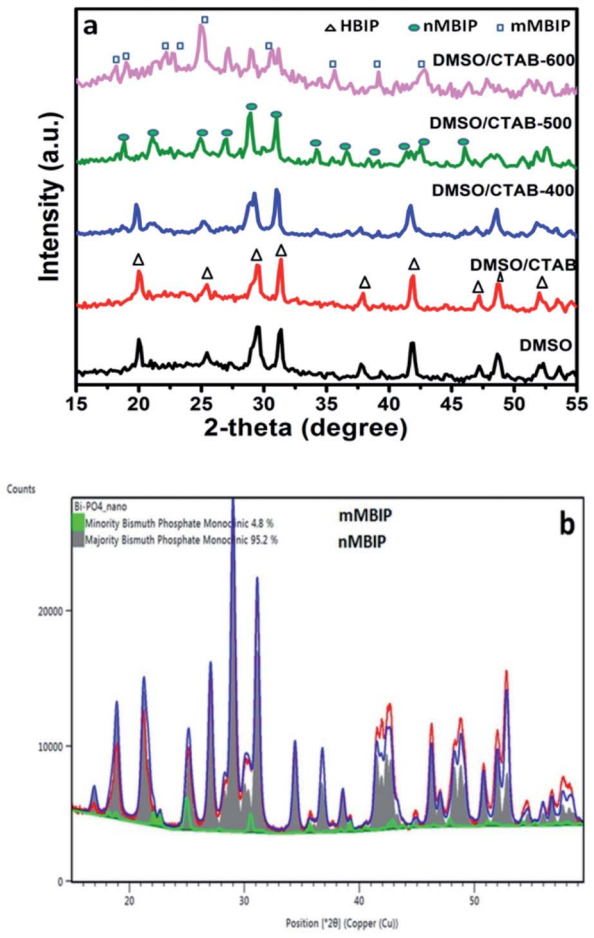

Fig. 1 (a) Powder XRD patterns of $BiPO_4$ synthesized in DMSO, DMSO/CTAB, and calcination of DMSO/CTAB at different temperatures 400–600 °C, (b) XRD pattern along with Rietveld refinements for $BiPO_4$ calcined at 500 °C.

(400–600 °C) for 2 h with heating rate 2 °C min^{-1}. It was found that, $BiPO_4$ calcined at 400 °C still displays the major hexagonal phase (HBIP) and some minor monazite monoclinic $BiPO_4$ (nMBIP) phase was detected. When the calcination was increased to 500 °C, XRD data indicates the phase junction formation of major (nMBIP) and minor (mMBIP). The diffraction peaks at 18.9°, 21.2°, 25.09°, 27.12°, 29.02°, 30.09°, 31.14°, 34.43°, 36.84°, 38.5°, 41.61°, 42.57°, and 46.21° associated with monazite monoclinic (nMBIP, JCPDS card no. 89-0287)[24] and those at 22.14°, 22.93°, 25.17°, 30.74° attributed to mMBIP (JCPDS card no. 77-2208).[25] Separation of the two monoclinic phases obtained at 500 °C was examined by Rietveld refinements as shown in Fig. 1b. It is clearly shown that the percentage of nMBIP and mMBIP is 95.2% and 4.8%, respectively. In addition, no peaks attributed to hexagonal $BiPO_4$ phase appeared at 500 °C. At 600 °C calcination temperature, the two monoclinic phase structures (nMBIP and mMBIP) existed simultaneously. However, the proportion of mMBIP more than that of nMBIP phase at 600 °C. This illustrates the formation of $BiPO_4$ phase structures (nMBIP and mMBIP) *via* calcination in the range from 500–600 °C as reported previously in the literature.[25] These results suggest that polymorphic $BiPO_4$ form can be selectively controlled by varying calcination temperature.

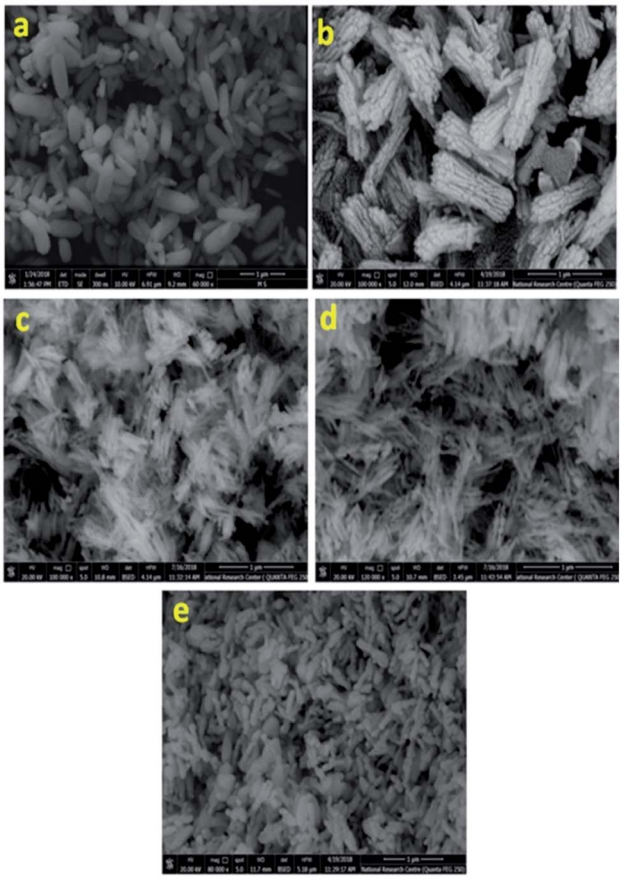

Fig. 2 SEM images of $BiPO_4$ prepared in DMSO (a), DMSO/CTAB (b), and calcined DMSO/CTAB at 400 °C (c), 500 °C (d), and 600 °C (e).

Fig. 2 presents the SEM images for all samples, clearly, nanorods-like morphology $BiPO_4$ were formed in DMSO. The diameters of nanorods is about 30 to 200 nm, and 500 nm in lengths as seen in Fig. 2 a. Further, the synthesized $BiPO_4$ sample in DMSO/CTAB shows nanorod bundles with 300 nm in diameter, and 800 nm in lengths as seen in Fig. 2b. These results illustrate the critical significant role of CTAB as surfactant in controlling the $BiPO_4$ morphology. Many cracks were observed on the surface which might be related to the growth defect. The FE-SEM image of $BiPO_4$ sample calcined at 400 °C revealed the spindle like-morphology with a highly fused state (Fig. 2c). Further increasing the temperature to 500 °C and 600 °C, the nanorod bundles-like morphology was converted to clusters as seen in Fig. 2(d and e), respectively.

The TEM image of $BiPO_4$ sample prepared in DMSO/CTAB showed that $BiPO_4$ formed as bundles-like morphology self-assembled by nanorods (Fig. 3a). The diameter of nanorod ranged from 30–40 nm as seen in Fig. 3a. HRTEM image of $BiPO_4$ nanorod bundles exhibited that the fringe spacing is 0.349 nm (Fig. 3b). This spacing related to (110) lattice plane of the hexagonal $BiPO_4$ (HBIP) phase (JCPDS card no. 15-0766) as shown in Fig. 3b. SAED pattern displayed a concentric ring shape, which confirms the polycrystalline sample in nature as presented in (Fig. 3c). TEM image of the $BiPO_4$ (nMBIP–mMBIP) calcined at 500 °C revealed the clusters nanorods were formed with diameters varying from 30 to 50 nm as seen in Fig. 3d. The corresponding HR-TEM image (Fig. 3e) shows a fringe spacing 0.417 nm, that agreed with (−111) lattice plane of nMBIP (JCPDS card no. 89-0287), and 0.390 nm which ascribed to (011) lattice plane of mMBIP (JCPDS card no. 77-2208). It is clearly demonstrated that the $BiPO_4$ phase structure (nMBIP and mMBIP) was formed. The corresponding (SAED) pattern showed the concentric rings as presented in Fig. 3f. Moreover,

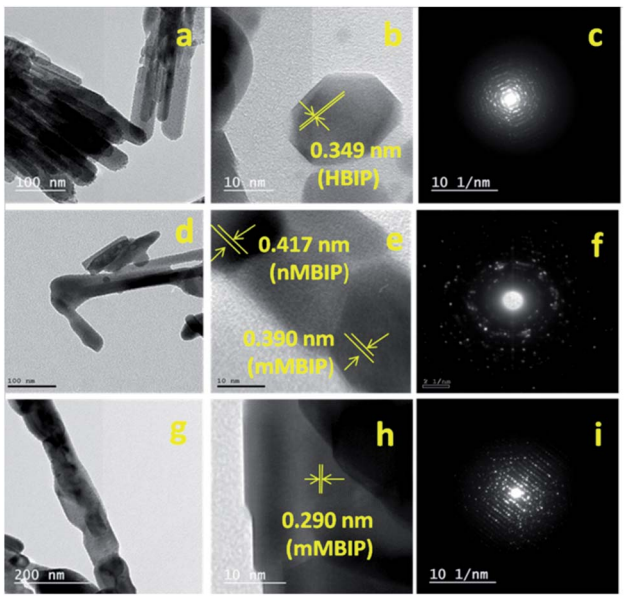

Fig. 3 TEM, HRTEM images and SEAD pattern of $BiPO_4$ prepared in DMSO/CTAB (a, b, and c, respectively), calcined DMSO/CTAB at 500 °C (d, e, and f, respectively), and the corresponding at 600 °C (g, h, i, respectively).

TEM image of the $BiPO_4$ calcined at 600 °C (Fig. 3g) shows clusters nanorods with diameter of 100 nm which is larger than that calcined at 500 °C. HRTEM image (Fig. 3h) revealed that the lattice fringe spacing is 0.290 nm, and matched with (111) lattice plane of mMBIP (JCPDS card no. 77-2208). The corresponding of a selected clusters nanorods (Fig. 3i) showed a regular arrays, indicates a single crystal structure. These results are well agreed with XRD data. Fig. S1† presents an image about annular dark-field of $BiPO_4$ calcined at 500 °C. The EDS mapping of $BiPO_4$ calcined at 500 °C shows that the elemental compositions are Bi, P, and O elements, as shown in Fig. S1.†

The specific surface areas measured for $BiPO_4$ prepared in DMSO and BiPO4 calcined at 500 °C were 88.96, and 67.52 $m^2 g^{-1}$, respectively (Table S1, ESI†). As shown in a previous reports, a low specific surface area is the major problem for the practical use of in the environment.[18,26] However, we have been successfully synthesized $BiPO_4$ photocatalyst with larger surface area using DMSO as a solvent. Therefore, DMSO plays a dominate role for increasing surface area values. As seen, the $BiPO_4$ prepared in DMSO has a larger surface area than $BiPO_4$ calcined at 500 °C. The decreasing in surface area after calcination at 500 °C is due to the highly fused state morphology as depicted in SEM and TEM images (Fig. 2 and 3).

The valence states of the elements were identified by the XPS. The full survey confirms the presence of Bi, P and O in $BiPO_4$ calcined at 500 °C (Fig. 4a). The peaks appeared at 158.16 and 163.46 eV are due to Bi $4f_{7/2}$ and Bi $4f_{5/2}$, respectively as shown in Fig. 4b.[3] The separation distance between Bi $4f_{7/2}$ and Bi $4f_{5/2}$ peaks is 5.3 eV, implying for Bi^{3+}.[27] The peak located at 131.51 eV is characterized to P 2p in $BiPO_4$ (Fig. 4c).[28] Moreover, the two peaks at 529.28 and 530.25 eV are related to O 1 s in crystal lattice, and (–OH) group, respectively as presented in Fig. 4d.[29,30]

FT-IR spectroscopy was performed on $BiPO_4$ samples to investigate the chemical bonding as seen in Fig. S2.† For $BiPO_4$ (HBIP) prepared in DMSO or DMSO/CTAB revealed that the peaks at 587 and 534 cm^{-1} correspond to asymmetric bending of δ (O–P–O) and ν_4 (PO_4), respectively.[31] the band located at 974 cm^{-1} referred to ν_3 (PO_4) asymmetric stretching. The hydroxyl band located at 1602 cm^{-1} is characterized to δ (H–O–H) bending modes of H_2O. The absorption band of hydroxyl stretching ν (O–H) centered at 3495 cm^{-1} (data not shown) was assigned to H_2O coordinated with the bismuth atoms. Upon calcination of HBIP at 400 °C, the stretching modes of PO_4 group were changed and slightly splitted to four absorption bands. These absorption bands at 1064, 986, 951 and 918 cm^{-1} are gradually strengthened with increasing the calcinations from 400 to 600 °C, implying the transformation of hexagonal $BiPO_4$ phase (HBIP) to monoclinic $BiPO_4$ phase (MBIP).[22] The band located at 534 cm^{-1} is splitted into four bands (494, 512, 527, and 549 cm^{-1}) after HBIP calcination at 500 and 600 °C, which attributes to asymmetric bending (ν_4) vibrations of PO_4 group.[25] This splitting revealed the transformation of HBIP to MBIP phase. Moreover, the band at 587 cm^{-1} of HBIP sample is slightly shifted to 599 cm^{-1} after calcination at 500 and 600 °C, which may be explained by the rotation of the PO_4 tetrahedron. The bending vibrations for O–H group nearly disappeared with increasing the calcination up to 500 and 600 °C.

The Raman spectra of $BiPO_4$ samples prepared in DMSO, DMSO/CTAB, and calcination temperature at 400, 500, 600 °C are presented in Fig. 5. The observed two bands at 969, and 1057 cm^{-1} for $BiPO_4$ synthesized in DMSO or DMSO/CTAB can be attributed to ν_1 symmetric stretching, and ν_3 asymmetric stretching of the PO_4 group, respectively.[32] The peaks at 590, 551, 447, and 403 cm^{-1} refer to the ν_4 and ν_2 (PO_4) bending modes.[33] The band at 204 cm^{-1} is due to (O–Bi–O) symmetric bending mode.[34] Obviously, calcination of HBIP indicated a significant changes in the Raman spectra. Under calcination of HBIP at 400 °C, the ν_3 asymmetric stretching band showed a blue shift to 1042 cm^{-1}, and slightly increased to 1037 cm^{-1} with increasing the calcination to 500 and 600 °C. In addition at 500 °C calcination temperature, the stretching mode of Bi–O located at 168 and 240 cm^{-1} are attributed to monoclinic Bi–O polyhedra.[25] The Raman peaks ascribed to monoclinic phase are relatively narrow than that of hexagonal phase.[35] The two bands at 918 and 277 cm^{-1} appeared after calcination at 500 °C

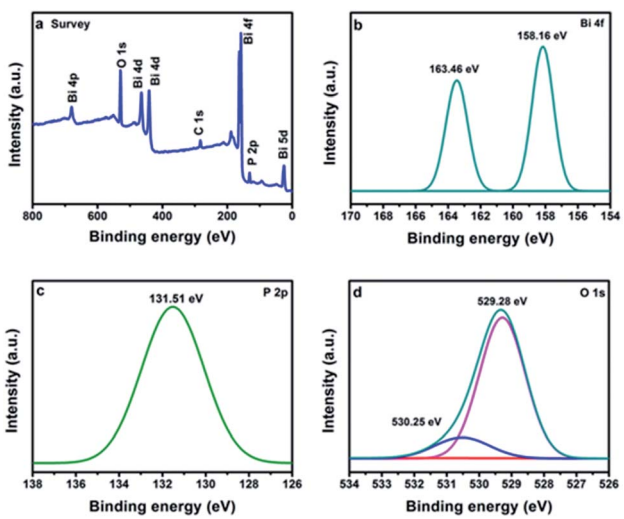

Fig. 4 XPS spectra of $BiPO_4$ calcined at 500 °C, survey (a), Bi 4f (b), P 2p (c), O 1s (d).

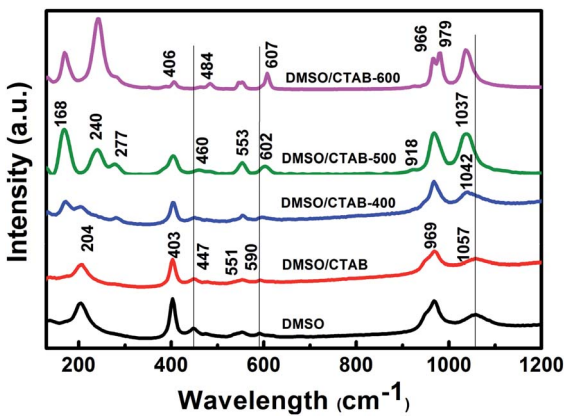

Fig. 5 Raman spectra of $BiPO_4$ prepared in DMSO, DMSO/CTAB, and calcination at 400 °C, 500 °C, and 600 °C.

corresponding to the ν_1 (PO_4) symmetric stretching band and (Bi–O) stretching modes, respectively.[15] These two bands are characteristic for the nMBIP. At the same time, the ν_4 and ν_2 bending modes of PO_4 group indicated a red shift to 602 and 460 cm^{-1}, respectively. Further, calcination at 600 °C, the ν_1 (PO_4) symmetric stretching mode is splitted into two peaks at 966, and 979 cm^{-1}. In addition, the bending modes of O–P–O displayed a significant red shift to 406, 484, and 607 cm^{-1}, these features appeared at 600 °C are related to the mMBIP phase.

The Raman analysis is agreed with XRD, HR-TEM, and FT-IR analysis which indicates the transformation of HBIP to nMBIP and to mMBIP phase under calcination temperature effect.

The UV-Vis diffuse reflectance for HBIP and MBIP samples were presented in Fig. 6a. The absorption band of HBIP initiates at 310 nm. Moreover, it was found that $BiPO_4$ under calcination at different temperatures shows optical absorption at 350 nm. The optical band gap (E_g) of the samples was evaluated using the Kubelka–Munk function as follow:[36]

$$(F(R)h\nu)^{0.5} = A(h\nu - E_g)$$

where $F(R)$, h, ν, A, E_g are diffuse reflection, Planck constant, vibration frequency, proportionality constant, and band gap, respectively. As presented in Fig. 6b, the energy band gap value was estimated using a Tauc model. The relation between $(F(R)h\nu)^{0.5}$ *versus* $h\nu$ related to indirect transition. The energy band gap of $BiPO_4$ synthesized in DMSO, DMSO/CTAB and calcined DMSO/CTAB at 400, 500, 600 °C were approximately at 4.45, 4.41, 4.30, 4.29, and 4.38 eV, respectively. Therefore, the band gap of calcined samples was lower than that of pure HBIP samples. This is might be due to the charge transferring between different $BiPO_4$ phase structures.

Fig. 7 shows the PL spectra at room temperature for $BiPO_4$ samples prepared in DMSO, DMSO/CTAB, and calcined $BiPO_4$ at different temperatures. The emission spectra appeared at about 468 nm. The hexagonal $BiPO_4$ sample prepared in DMSO exhibited the highest emission peak intensity compared to others, indicates the highest electron–hole pairs recombination rate. In contrast, the calcined of $BiPO_4$ at 500 °C exhibited the weakest emission peak intensity, this might be attributed to the surface phase junction formation in monoclinic $BiPO_4$, which revealing the lowest charges recombination rate. Consequently, these results prove that the presence of surface phase junction has diminished the rate of recombination between charges transfer and thus expected to improve the behavior of photocatalytic.

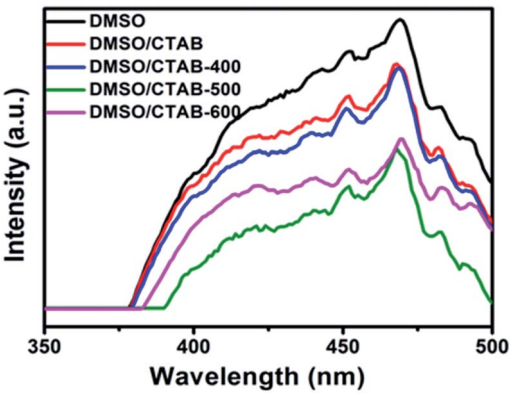

Fig. 7 PL spectra of $BiPO_4$ synthesized in DMSO, DMSO/CTAB, and calcination of DMSO/CTAB at different temperatures.

3.2 Photocatalytic performance

Aniline blue (AB) degradation reactions were carried out under UV light to investigate the photocatalytic behavior of the $BiPO_4$ samples. As presented in Fig. 8a, no degradation of AB was observed without photocatalyst addition under UV light irradiation, indicating the stability of aniline blue and its photolysis difficulty. In addition, it was found that 46.26, 53.78, 58.82, 91.12, and 70% of aniline blue were degraded after 180 min in the presence of $BiPO_4$ photocatalyst prepared in DMSO, DMSO/CTAB, and calcined at 400, 500, 600 °C, respectively. Clearly, hexagonal $BiPO_4$ samples prepared in (DMSO or DMSO/CTAB) displayed lower photocatalytic activity compared to monoclinic phase as reported before.[20] With increasing the $BiPO_4$ calcination, aniline blue degradation rate are improved. Surprisingly, when the calcination temperature rise to 600 °C, the AB degradation rate was decreased. Meanwhile, the calcined $BiPO_4$ at 500 °C showed the highest catalytic activity compared to others samples. This illustrates the higher proportion of nMBIP than mMBIP at 500 °C as discussed in (Rietveld refinement method), which exhibited higher catalytic activity.[37] This finding demonstrates that nMBIP phase with the most distorted PO_4 tetrahedron possess the highest photocatalytic activity toward pollutants degradation. Fig. 8b shows the temporal

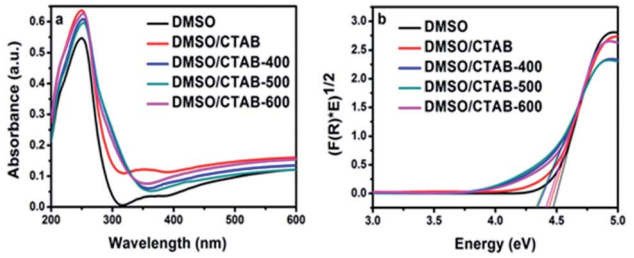

Fig. 6 (a) UV-Vis diffuse reflection spectrum of $BiPO_4$ synthesized in DMSO, DMSO/CTAB, and calcination of DMSO/CTAB at different temperatures; (b) Tauc plots ($(F(R)h\nu)^{0.5}$ *vs.* $h\nu$) constructed from Fig. 6a.

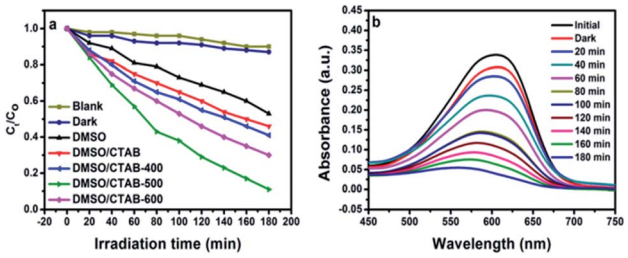

Fig. 8 (a) Degradation rate of AB over all as-synthesized $BiPO_4$ samples; (b) changes in the temporal UV-Vis absorption spectrum during the photodegradation of AB in aqueous solution over calcined $BiPO_4$ at 500 °C.

absorption spectral changes of AB using calcined $BiPO_4$ at 500 °C. During the photodegradation reactions, the absorption peak intensity at 606 nm reduced gradually, and about 91.12% of AB could be degraded after 180 min.

The crystal structures of $BiPO_4$ calcined at 500 °C clearly shows that the change in distortion of polyhedron (Bi–O) and tetrahedron (P–O) is attributed to the symmetry of the crystal structures as shown in Fig. S3.† The bond length in Bi–O and P–O of nMBIP are dispersed broadly more than mMBIP.[38] Therefore, the improvement in photocatalytic activities is related to crystal structures of $BiPO_4$.

The photocatalytic behavior was assigned to the first-order kinetics of Langmuir–Hinshelwood model as follows.[39]

$$\ln(C_t/C_0) = -k_{app}t$$

where k_{app}, t is the apparent first-order rate constant (min^{-1}), and time, respectively. The k_{app} value was estimated from the slope between $\ln(C_t/C_0)$ *versus* time (t), as presented in Fig. 9a.

The rate constant of $BiPO_4$ calcined at 500 °C was 0.0113 min^{-1} as shown in Fig. 9b. This was 3.4 and 2.8 times more than that of $BiPO_4$ prepared in DMSO (k_{app} 0.0033 min^{-1}) or DMSO/CTAB (k_{app} 0.004 min^{-1}), respectively. This behavior was thought to be due to the formation of $BiPO_4$ phases (nMBIP–mMBIP) at 500 °C which enhance the charges transfer, thus improved the photocatalytic performance.

3.3 Photodegradation mechanism

Different scavengers have been added during the oxidation reactions to determine the oxidative species in the photocatalytic system. EDTA-2Na and *t*-BuOH were selected as the hole and radical scavenger, respectively.[40] Obviously, the AB degradation rate was significantly suppressed by using EDTA-2Na, and/or *t*-BuOH indicating that the holes and radicals are mainly oxidative species as shown in Fig. 10a. The k_{app} value with various scavengers is estimated from the relation between $\ln(C_t/C_0)$ *versus* time (t) as shown in Fig. 10b. The change in the rate constant with addition of scavengers was indicated as presented in Fig. 10c. It can be seen that the presence of EDTA-2Na and/or *t*-BuOH show a significant effect in decreasing k_{app}. In contrast, sample performed in the absence of scavengers has the highest k_{app} value, confirming the dominant role of holes and radicals in the phase junction system. The electron–hole pairs separation over $BiPO_4$ phase junction system is shown in

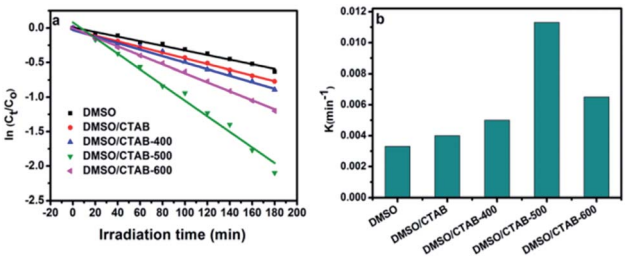

Fig. 9 (a) Linear transform $\ln(C_t/C_0) = f(t)$ of the AB degradation kinetics curves; (b) first-order rate constant of all as-synthesized $BiPO_4$ samples.

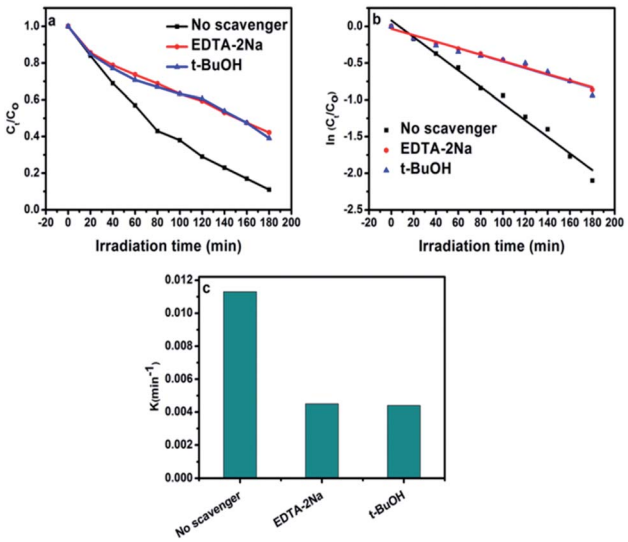

Fig. 10 (a) Photocatalytic degradation of AB over calcined $BiPO_4$ at 500 °C with various scavengers EDTA-2Na, and *t*-BuOH; (b) linear transform $\ln(C/C_0) = f(t)$ of the AB degradation kinetics curves under different scavenger; (c) comparison of photocatalytic activity obtained using the rate constant k_{app} with different scavengers.

Scheme 1. The transferring of the charges mainly depends on the band potential, which theoretically estimated using electronegativity concept.[26,41] The photocatalyst band potential can be evaluated as follows:[42]

$$E_{VB} = X - E_e + 0.5E_g$$

$$E_{CB} = E_{VB} - E_g$$

where E_{VB}, E_{CB}, X, E_e, E_g is the valence band potential, the conduction band potential, electronegativity of the $BiPO_4$ photocatalyst interface (6.860 eV (ref. 26)), energy of free electron (4.5 eV), and the band gap of $BiPO_4$, respectively. As presented in Scheme 1, both the E_{VB} and E_{CB} of nMBIP was found between the energy gap of mMBIP, forming a straddling band "type I" phase junction. Under UV-light, the electrons on the

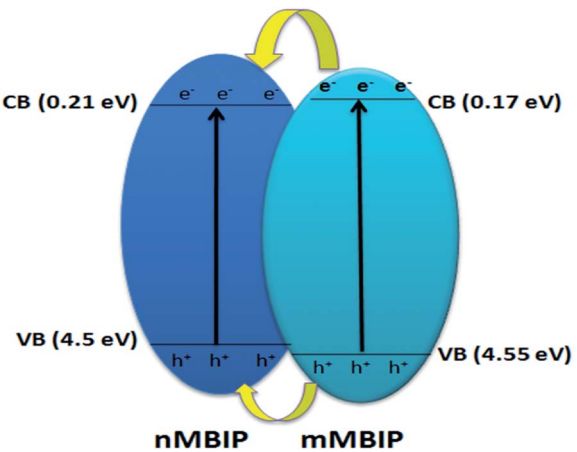

Scheme 1 Schematic diagram shows the electron–hole separation over $BiPO_4$ phase junction system under UV light irradiation.

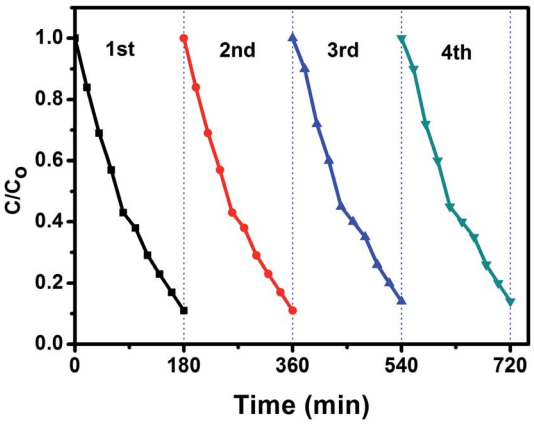

Fig. 11 Recycling tests on calcined $BiPO_4$ at 500 °C for the degradation of AB under UV irradiation.

conduction band (mMBIP) moved to the conduction band (nMBIP) and could reduce (O_2) formed on the phase junction surface to $^{\bullet}O^{2-}$. Therefore, the $^{\bullet}O^{2-}$ could decompose the AB dye. In addition, the holes on the valence band (mMBIP) are transferred to the valence band (nMBIP), which react with H_2O and produce $^{\bullet}OH$ radicals, subsequently the $^{\bullet}OH$ could decompose the AB dye. Therefore, we can conclude that the phase junction formation of nMBIP–mMBIP is responsible for the photocatalytic activity enhancement.

3.4 Stability evaluation

The stability and reusability is an important parameter of the photocatalytic process. In order to investigate the photocatalytic stability of the photocatalyst, the circulation runs for photocatalytic degradation of aniline blue (AB) with the $BiPO_4$ phase junction (nMBIP–mMBIP) calcined at 500 °C are carried out to evaluate its cycling stability.

Prior to the next cycle experiment, the previously used photocatalyst is subjected to washed with distilled water, dried at 90 °C, added to 100 ml of (AB) dye (20 ppm), and irradiated under UV light. After each 20 min, approximately 3 ml liquid sample was withdrawn, centrifuged, and measured using spectrophotometer instrument. As seen in Fig. 11, the photocatalytic performance was monitored for four successive cycles. The activity was decreased slightly up to 85% in the fourth cycle. This indicates that nMBIP–mMBIP phase junction displays high stability and no photocorrosion occurred during the photocatalytic oxidation process.

4. Conclusions

Hexagonal $BiPO_4$ photocatalyst has been fabricated by a facile precipitation route using DMSO as a solvent. By using surfactant (CTAB), $BiPO_4$ nanorod bundles could be obtained, revealing the controlling of $BiPO_4$ morphology. Calcinating the hexagonal $BiPO_4$ at different temperatures was also discussed. $BiPO_4$ calcined at 500 °C indicated the superior performance for AB degradation and its rate constant was 3.4 times higher than that by HBIP. The nMBIP–mMBIP phase junction system facilities the separation of the photogenerated e^-/h^+ pairs, thus enhanced the behavior of photocatalytic. The results provide that nMBIP verifies the dominate role for enhancing the performance of photocatalytic rather than mMBIP.

Conflicts of interest

There are no conflicts to declare.

Acknowledgements

This study was partly supported by Central Metallurgical Research and Development Institute (CMRDI), Egypt project no. 39/2108 and Massachusetts Institute of Technology (MIT), USA.

Notes and references

1 Y. Wang, B. Li, G. Li, X. Ma, H. Zhang, Y. Huang, G. Wang, J. Wang and Y. Song, *Chem. Eng. J.*, 2017, **322**, 556–570.
2 D. Yuan, L. Huang, Y. Li, Y. Xu, H. Xu, S. Huang, J. Yan, M. He and H. Li, *RSC Adv.*, 2016, **6**, 41204–41213.
3 J. Wang, J. Jin, X. Wang, S. Yang, Y. Zhao, Y. Wu, S. Dong, J. Sun and J. Sun, *J. Colloid Interface Sci.*, 2017, **505**, 805–815.
4 X. Zou, C. Ran, Y. Dong, Z. Chen, D. Dong, D. Hu, X. Li and Y. Cui, *RSC Adv.*, 2016, **6**, 20664–20670.
5 H. Sun, G. Zhou, Y. Wang, A. Suvorova and S. Wang, *ACS Appl. Mater. Interfaces*, 2014, **6**, 16745–16754.
6 M. Wei, L. Gao, J. Li, J. Fang, W. Cai, X. Li and A. Xu, *J. Hazard. Mater.*, 2016, **316**, 60–68.
7 T. Wu, P. Wang, J. Qian, Y. Ao, C. Wang and J. Hou, *Dalton Trans.*, 2017, **46**, 13793–13801.
8 M. Yan, Y. Wu, Y. Yan, X. Yan, F. Zhu, Y. Hua and W. Shi, *ACS Sustainable Chem. Eng.*, 2016, **4**, 757–766.
9 F. Kiantazh and A. Habibi-Yangjeh, *Solid State Sci.*, 2015, **49**, 68–77.
10 S. M. El-sheikh, T. M. Khedr, G. Zhang, V. Vogiazi, A. A. Ismail, K. O. Shea and D. D. Dionysiou, *Chem. Eng. J.*, 2017, **310**, 428–436.
11 G. Zhang, Y. C. Zhang, M. Nadagouda, C. Han, K. O'Shea, S. M. El-Sheikh, A. A. Ismail and D. D. Dionysiou, *Appl. Catal., B*, 2014, **144**, 614–621.
12 S. M. El-Sheikh, T. M. Khedr, A. Hakki, A. A. Ismail, W. A. Badawy and D. W. Bahnemann, *Sep. Purif. Technol.*, 2017, **173**, 258–268.
13 P. Madhusudan, J. Ran, J. Zhang, J. Yu and G. Liu, *Appl. Catal., B*, 2011, **110**, 286–295.
14 C. Pan and Y. Zhu, *Environ. Sci. Technol.*, 2010, **44**, 5570–5574.
15 Y. Zhiu, Y. Liu, Y. Lv, Q. Ling, D. Liu and Y. Zhu, *J. Mater. Chem. A*, 2014, **2**, 13041–13048.
16 N. Mohaghegh, M. Tasviri, E. Rahimi and M. R. Gholami, *RSC Adv.*, 2015, **5**, 12944–12955.
17 V. A. Online, X. Jia, J. Cao, H. Lin, M. Zhang, X. Guo and S. Chen, *RSC Adv.*, 2016, **6**, 55755–55763.
18 L. She, G. Tan, H. Ren, J. Huang, C. Xu and A. Xia, *RSC Adv.*, 2015, **5**, 36642.

19 J. Zhang, Q. Xu, Z. Feng, M. Li and C. Li, *Angew. Chem., Int. Ed.*, 2008, **47**, 1766–1769.
20 C. Pan and Y. Zhu, *Catal. Sci. Technol.*, 2015, **5**, 3071–3083.
21 Y. Cao, N. Liu, J. Tian, Y. Liu and X. Zhang, *Chem. Phys. Lett.*, 2015, **640**, 180–183.
22 M. Zhao, G. Li, J. Zheng, L. Li, H. Wang and L. Yang, *CrystEngComm*, 2011, **13**, 6251.
23 Y. Guo, P. Wang, J. Qian, Y. Ao, C. Wang and J. Hou, *Appl. Catal., B*, 2018, **234**, 90–99.
24 J. Li, H. Yuan and Z. Zhu, *RSC Adv.*, 2016, **6**, 70563–70572.
25 M. H. Fulekar, A. Singh, D. P. Dutta, M. Roy, A. Ballal and A. K. Tyagi, *RSC Adv.*, 2014, **4**, 10097–10107.
26 Y. Liu, P. Zhang, H. Lv, J. Guang, S. Li and J. Jiang, *RSC Adv.*, 2015, **5**, 83764–83772.
27 Y. Yan, Z. Zhou, W. Li, Y. Zhu, Y. Cheng, F. Zhao and J. Zhou, *RSC Adv.*, 2014, **4**, 38558–38567.
28 M. Lu, G. Yuan, Z. Wang, Y. Wang and J. Guo, *Nanoscale Res. Lett.*, 2015, **10**, 1–7.
29 M. Wang, Y. Che, C. Niu, M. Dang and D. Dong, *J. Hazard. Mater.*, 2013, **262**, 447–455.
30 J. Li, H. Yuan and Z. Zhu, *Appl. Surf. Sci.*, 2016, **385**, 34–41.
31 Y. Zhang, B. Shen, H. Huang, Y. He, B. Fei and F. Lv, *Appl. Surf. Sci.*, 2014, **319**, 272–277.
32 G. Li, Y. Ding, Y. Zhang, Z. Lu, H. Sun and R. Chen, *J. Colloid Interface Sci.*, 2011, **363**, 497–503.
33 J. Li, H. Yuan and Z. Zhu, *J. Alloys Compd.*, 2015, **640**, 290–297.
34 G. Lakshminarayana, T. D. Dao, K. Chen, M. Sharma, T. Takeda, M. G. Brik, I. V. Kityk, S. Singh and T. Nagao, *Opt. Mater.*, 2015, **39**, 110–117.
35 M. Zhao, G. Li, L. Li, L. Yang and J. Zheng, *Cryst. Growth Des.*, 2012, **12**, 3983–3991.
36 F. Feng, W. Yang, S. Gao, C. Sun and Q. Li, *ACS Sustainable Chem. Eng.*, 2018, **6**, 6166–6174.
37 L. Zhu, X.-G. Ma, Y. Wei, L. Chu, H.-H. Wang and C.-Y. Huang, *Chin. J. Struct. Chem.*, 2017, **36**, 1299–1306.
38 C. Pan, D. Li, X. Ma, Y. Chen and Y. Zhu, *Catal. Sci. Technol.*, 2011, **1**, 1399–1405.
39 L. She, G. Tan, H. Ren, J. Huang, C. Xu and A. Xia, *RSC Adv.*, 2015, **5**, 36642–36651.
40 Y. Zhang, H. Fan, M. Li and H. Tian, *Dalton Trans.*, 2013, **42**, 13172.
41 H. Xu, Y. Xu, H. Li, J. Xia, J. Xiong, S. Yin, C. Huang and H. Wan, *Dalton Trans.*, 2012, **41**, 3387.
42 F. Duo, Y. Wang, X. Mao, X. Zhang, Y. Wang and C. Fan, *Appl. Surf. Sci.*, 2015, **340**, 35–42.